Environmental Modelling and Software 149 (2022) 105283

Contents lists available at ScienceDirect

Environmental Modelling and Software

journal homepage: www.elsevier.com/locate/envsoft

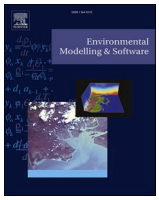

Virtual laboratory for understanding impact of heterogeneity on ecohydrologic processes across scales☆

Kunxuan Wang [a], Praveen Kumar [a,b,*]

[a] Department of Civil and Environmental Engineering, University of Illinois, Urbana, 61 801, IL, USA
[b] Department of Atmospheric Science, University of Illinois, Urbana, 61 801, IL, USA

ARTICLE INFO

Keywords:
Ecohydrologic modeling
3D flow model
Spatial variability
Graphical user interface

ABSTRACT

Hyper-resolution land surface models can explicitly represent landscape scale heterogeneity, but the complexity of representing finer scale processes and meeting computational needs makes them inaccessible to the general scientific community and limits their adoption. In this work, we present the Multi-layer Canopy and 3D Soil (MLCan3D) model, which is a high resolution, high fidelity, physical ecohydrologic model that aims to maintain accessibility. MLCan3D implements detailed physical process representations, is accessible through graphical user interface, and is tested using comparisons with other models and field data. This work demonstrates the feasibility of using MLCan3D to produce simulations close to real systems and the potential of the model to perform virtual experiments to explore model results. Our goal is for MLCan3D to serve as a virtual laboratory that enables virtual experiments from the broader scientific community and contribute to our understanding of ecohydrologic process heterogeneity, dynamics, and interactions across scales.

1. Introduction

Modeling of ecohydrologic processes is important in quantifying the water resource dynamics such as prediction of floods and droughts, and, among others, in understanding vegetation processes and ecosystem carbon fluxes. Accurate quantification of land surface processes is also important for weather and climate predictions because of the strong interaction and feedback between land surface and atmospheric processes (Walker and Rowntree, 1977; Shukla et al., 1990). Fine scale ecohydrologic heterogeneity such as those related to topography, soil moisture and water flux has been shown to significantly influence larger scale ecosystem water and energy fluxes (Le and Kumar, 2017; Riley and Shen, 2014; Vivoni et al., 2010), runoff and streamflow (Arrigo and Salvucci, 2005; Barrios and Francés, 2012), and atmospheric feedback and circulation (Nykanen and Foufoula-Georgiou, 2001). Current models tend to focus on their ability to simulate large domains and computation efficiency. They make sacrifices such as simplification of process representations, reduction of process complexity and the range of processes captured, and are often limited by computing hardware constrains (Maxwell et al., 2015; Le et al., 2015). In this work, we present a high-resolution and high fidelity ecohydrologic model that focuses on detailed physical process representation, ease of use, and broad applicability to serve as a virtual laboratory. It is aimed to enable the general scientific community to use it to explore the interactions between topographic variability and ecohydrologic processes where complex feedback between these processes lead to non-linear ecohydrologic dynamics.

With recent advances in environmental data availability and computational capability, there is a call for hyper-resolution land surface models over the regional to global extent that can more explicitly represent ecohydrologic heterogeneity to better understand and predict the non-linear interactions between spatial variability and ecohydrologic processes (Bierkens et al., 2015; Wood et al., 2011). Hydrologic and land surface models are starting to become available at the ~100 m resolution for continental extent and ~1 km resolution for global extent (Maxwell et al., 2015; Sutanudjaja et al., 2018; de Graaf et al., 2017). Subgrid-scale processes, such as those associated with micro-topographic variability, are generally simplified with subgrid parameterizations or ignored (Clark et al., 2015). However, current understanding and model representation of many ecosystem processes are developed and validated with sensor measurements at the meter scale (Wood et al., 2011), and understanding and quantifying how

☆ MLCan3D is open source and available at https://github.com/HydroComplexity/MLCan3D.

* Corresponding author. Department of Civil and Environmental Engineering, University of Illinois, Urbana, 61 801, IL, USA.
E-mail address: kumar1@illinois.edu (P. Kumar).

https://doi.org/10.1016/j.envsoft.2021.105283
Received 10 November 2021; Accepted 8 December 2021
Available online 16 December 2021

processes behave at the ~100 m scale remains an issue (Clark et al., 2015). Some hypothesize that current model formulations relating to ecohydrologic processes are applicable and meaningful up to ~100 m resolution as the limit (Wood et al., 2011; Riley and Shen, 2014). However, other works find that meter scale micro-topographic features influence stream flow (Dunne et al., 1991; Frei et al., 2010; Thompson et al., 2010), infiltration (Frei and Fleckenstein, 2014; Le and Kumar, 2017), and vegetation (McGrath et al., 2012). Therefore, micro-topographic variability is important for better understanding of heterogeneous ecohydrologic processes and how they behave at larger scales.

In order to better understand the complex interactions between topographic variability and ecohydrologic processes, we need models that can capture the influence of micro-topographic variability and represent physical processes that couples heterogeneity with other ecohydrologic dynamics. While such models are starting to emerge, the increases in model resolution, fidelity of process representation, and range of processes represented incur significant computational costs. Many models prioritize the ability to simulate large domains and efficient computation, (Maxwell et al., 2015; Le and Kumar, 2017), and they are effective for their purpose and necessary for advancement of the science. However, to meet computation needs, they may simplify process representations and reduce process representations and couplings. They also extensively leverage advanced hardware and computation methods, and thus tend to be less accessible to general scientific community due to the learning curve needed to set up the models, complexity of the code, and limiting knowledge to exploit advanced hardware such as hybrid computing involving both CPU (central processing units) and GPU (graphical processing units) (Le and Kumar, 2017). Due to such complexity, these models are also often only tested on individual or limited number of sites (Baatz et al., 2018), further limiting their adoption by general users. In order to stimulate scientific exploration of how fine scale landscape heterogeneity affects ecohydrologic process dynamics, a model that overcomes the above issues and focuses on physical process representation, greater accessibility, and wider applicability is needed.

Therefore, in this work, we present the Multi-layer Canopy and 3D Soil (MLCan3D) model: a high-resolution, high fidelity, but easy to use ecohydrologic model for simulating heterogeneities from micro-topographic scale to larger scales and their interactions with coupled ecohydrologic processes. Our goal is to provide an accessible model for the general scientific community that can be used as a virtual laboratory for testing scientific hypotheses, investigating knowledge gaps, and understanding ecohydrologic process interactions and dynamics (Fatichi et al., 2016). In MLCan3D, we implement topography aware surface and subsurface moisture dynamics with 2D diffusive overland flow and 3D terrain-following Richards' Equation for subsurface flow. We model vegetation, energy, and above-ground moisture processes with an advanced ecohydrologic process model, the Multi-Layer Canopy (MLCan) model, that has been tested on a wide range of ecosystems (Drewry et al., 2010a,b; Quijano et al., 2012, 2013; Quijano and Kumar, 2015). We tightly integrate our state of the art 3D flow model with MLCan through root-soil moisture exchange and fully coupled surface flow and land surface water and energy processes. To keep the model accessible, we improve upon the Graphical User Interface (GUI) developed for MLCan (Le et al., 2012) to facilitate model setup, and we use the Advanced Iterative Alternating Direction Implicit (AIADI) method (An et al., 2011; Douglas and Rachford, 1956) to solve the subsurface flow so that the model can be run without stringent computing hardware constraints. We simulate two very different ecosystems to test and demonstrate the broad applicability of MLCan3D.

With the availability of extensive ecohydrologic observations from observational networks such as the Critical Zone Observatories (CZOs) (Brantley et al., 2006), the Long-Term Ecosystem Research (LTER) network (Callahan, 1984), and the National Ecological Observatory Network (NEON) (National Research Council, 2004), we have the ability to develop simulations that capture real world behavior with high fidelity (Baatz et al., 2018). Based on these simulations, we can then perform virtual experiments to gain understanding about processes in temporal and spatial extents and resolutions that cannot be measurement in the field (Fatichi et al., 2016) or guide the design of new experiments. By focusing on process representation, accessibility, and wide applicability, we believe that MLCan3D can serve as a virtual laboratory that encourage such experiments by the scientific community.

In Section 2, we first discuss the theory, numerical implementation, and benchmark verification of the coupled surface-subsurface 3D flow model that captures topographic heterogeneity. Next, we discuss the integration of the flow model with the MLCan model in Section 3. Then in Section 4, we apply the model to two very different NEON sites to test and demonstrate model capability. We close with Sections 5 and 6 with discussion of model sensitivity, results, and next steps.

2. Surface-subsurface 3D flow model

2.1. 3D subsurface flow

In many diverse fields of study, Richards' equation is seen as the standard for modeling water flow in the near surface soil layers (Hillel, 2013). There are three forms of the equation used in existing studies, the 'h-based' form solving for pressure head, the 'θ-based' form solving for soil moisture, and the 'mixed-form' using both pressure and moisture as dependent variables. Studies have shown that the 'mixed-form' Richards' equation is perfectly mass conserved using finite difference and gives better performance over the other forms at no additional computational cost (Celia et al., 1990; An et al., 2011). Therefore, in this work, we use the 'mixed-form' Richards' equation that is generally written as follows (Celia et al., 1990):

$$\frac{\partial\theta}{\partial t} = \nabla\cdot K(\psi)\nabla\psi - \frac{\partial K}{\partial z}. \tag{1}$$

Here, θ is the volumetric soil moisture content. $K(\psi)$ is the unsaturated hydraulic conductivity which depends on soil matric potential ψ. The relationships between K, θ and ψ are calculated using the well known soil moisture retention curve from van Genutchen (Van Genuchten, 1980) and the unsaturated hydraulic conductivity function from Mualem (1976):

$$\Theta = \frac{\theta-\theta_r}{\theta_s-\theta_r} = \frac{1}{[1+(\alpha\psi)^{n_v}]^{m_v}}, \tag{2}$$

$$K(\Theta) = K_s\Theta^{1/2}[1-(1-\Theta^{1/m_v})^{m_v}]^2. \tag{3}$$

θ_r, θ_s are the residual and saturated soil moisture. K_s is the saturated hydraulic conductivity. α is a parameter corresponding to the inverse air-entry value. n_v is the pore-size distribution, and $m_v = 1 - 1/n_v$. All parameters can be found based on soil type or composition.

To generalize the Richards' equation to be applicable to model a natural environment, we modify Equation (1) to account for plant root uptake, elastic storage, and topography as follows:

$$\frac{\partial\theta}{\partial t} + \frac{\theta}{\varphi}S_s\frac{\partial h}{\partial t} = \nabla\cdot K(\psi)[\nabla h\cos\vartheta + \sin\vartheta] - q_t. \tag{4}$$

The inclusion of flux due to transpiration q_t accounts for vegetation root uptake. $\frac{\theta}{\varphi}S_s\frac{\partial h}{\partial t}$ accounts for elastic storage (Bear et al., 1979) where φ is the porosity, and S_s is elastic storage coefficient. To account for changes in elevation within the domain, we use h, the total pressure head, where $h = \psi + z$. ψ is the soil matric head as previously defined, and z is the gravity head, the elevation above a given datum. We further apply a terrain following transform to better account for topography in the domain (Maxwell, 2013; Childs, 1971; Sloan and Moore, 1984;

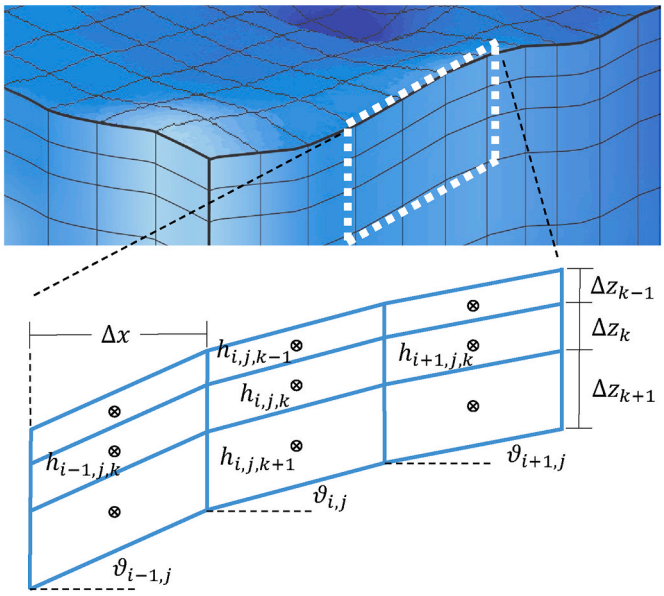

Fig. 1. In this figure, the top shows the grid formulation for the 3D subsurface model with terrain following transform. The bottom depicts a detailed 2D view of the discretization used in the finite difference solution. *i*, *j*, *k* are cell indices in the *x*, *y*, and *z* directions respectively. Horizontal grid size (Δx, Δy) are constant over space, but the depth of each layer (Δz) can vary.

Brutsaert, 1994). A representation of the 3D subsurface model with terrain following transform is shown at the top of Fig. 1. The terrain following transform $[\nabla h \cos\vartheta + \sin\vartheta]$ modifies horizontal fluxes to follow local topographic slope with angle ϑ assuming local slope is constant over depth. Angles of local slope in the horizontal directions are calculated as $\vartheta_x = \tan^{-1}(\frac{\partial z}{\partial x})$ and $\vartheta_y = \tan^{-1}(\frac{\partial z}{\partial y})$. Since there is no need to account for slope for vertical fluxes $\vartheta_z = 0$. Compared to traditional orthogonal fluxes, the terrain following implementation improves in accuracy and is better suited to modeling complex terrains or at coarse spatial resolutions (Maxwell, 2013).

We solve Equation (4) using Backward Euler for the time discretization and finite difference for space discretization. The bottom of Fig. 1 shows the finite difference stensil in the $x-z$ plane. Since the Richards' equation is non-linear due to the relationship between θ, K and h, we use the modified Picard method (Celia et al., 1990) to linearize the equation and solve each time step iteratively. Please refer to Appendix A.1 for more details on the discretization of Equation (4).

2.1.1. AIADI

Due to considerations for ease of use and computational effort, an ADI scheme is used to solve Equation (4) one dimension at a time instead of the full implicit solution. Previous studies have compared ADI with full implicit implementations for multi-dimensional Richards' Equation and found ADI method to be faster with similar simulation results (An et al., 2011). However, traditional ADI methods (Peaceman and Rachford, 1955; Rubin, 1968) can encounter instabilities and difficulty in convergence when solving higher dimension problems (Clement et al., 1994). To overcome these issues, we use the Advanced Iterative Alternating Direction Implicit (AIADI) method (An et al., 2011; Douglas and Rachford, 1956), which was first developed for linear parabolic partial differential equations and is unconditionally stable in 2D and 3D (Douglas and Rachford, 1956). In non-linear cases, stability is not guaranteed, but is improved over traditional ADI methods (An et al., 2011). We adapt the AIADI method to solve the generalized Richards' Equation (4) for natural environments.

Our modified AIADI method uses three passes as follows:

First pass in x-direction:

$$\begin{aligned}
&\frac{\theta^{n+1,3m}-\theta^{n}}{\Delta t}+\left(\frac{C^{n+1,3m}}{\Delta t}+I_m\overline{K}^{n+1,3m}\right)\\
&\cdot\left(h^{n+1,3m+1}-h^{n+1,3m}\right)+\frac{\theta^{n+1,3m}}{\varphi}\frac{S_s}{\Delta t}\left(h^{n+1,3m+1}-h^{n}\right)\\
&=\frac{\partial}{\partial x}\left[K^{n+1,3m}\left(\frac{\partial h}{\partial x}\Big|^{n+1,3m+1}\cos\vartheta_x+\sin\vartheta_x\right)\right]\\
&+\frac{\partial}{\partial y}\left[K^{n+1,3m}\left(\frac{\partial h}{\partial y}\Big|^{n+1,3m}\cos\vartheta_y+\sin\vartheta_y\right)\right]\\
&+\frac{\partial}{\partial z}\left(K^{n+1,3m}\frac{\partial h}{\partial z}\Big|^{n+1,3m}\right)-q_t,
\end{aligned}\tag{5}$$

second pass in y-direction:

$$\begin{aligned}
&\left(\frac{C^{n+1,3m}}{\Delta t}+I_m\overline{K}^{n+1,3m}+\frac{\theta^{n+1,3m}}{\varphi}\frac{S_s}{\Delta t}\right)\left(h^{n+1,3m+2}-h^{n+1,3m+1}\right)\\
&=\frac{\partial}{\partial y}\left[K^{n+1,3m}\left(\frac{\partial h}{\partial y}\Big|^{n+1,3m+2}\cos\vartheta_y+\sin\vartheta_y\right)\right]\\
&-\frac{\partial}{\partial y}\left[K^{n+1,3m}\left(\frac{\partial h}{\partial y}\Big|^{n+1,3m}\cos\vartheta_y+\sin\vartheta_y\right)\right]\\
&=\frac{\partial}{\partial y}\left(K^{n+1,3m}\frac{\partial h}{\partial y}\Big|^{n+1,3m+2}cos\,\vartheta_y\right)\\
&-\frac{\partial}{\partial y}\left(K^{n+1,3m}\frac{\partial h}{\partial y}\Big|^{n+1,3m}\cos\vartheta_y\right),
\end{aligned}$$

and third pass in z-direction:

$$\begin{aligned}
&\left(\frac{C^{n+1,3m}}{\Delta t}+I_m\overline{K}^{n+1,3m}+\frac{\theta^{n+1,3m}}{\varphi}\frac{S_s}{\Delta t}\right)\left(h^{n+1,3m+3}-h^{n+1,3m+2}\right)\\
&=\frac{\partial}{\partial z}\left(K^{n+1,3m}\frac{\partial h}{\partial z}\Big|^{n+1,3m+3}\right)\\
&-\frac{\partial}{\partial z}\left(K^{n+1,3m}\frac{\partial h}{\partial z}\Big|^{n+1,3m}\right),
\end{aligned}$$

where

$$\begin{aligned}
\overline{K}^{n}_{i,j,k}&=K^{n}_{i-1/2,j,k}+K^{n}_{i+1/2,j,k}+K^{n}_{i,j-1/2,k}+K^{n}_{i,j+1/2,k}\\
&+K^{n}_{i,j,k-1/2}+K^{n}_{i,j,k+1/2},
\end{aligned}$$

and

$$I_m=0.55^m.\tag{6}$$

Here n is the timestep index, and m is the Picard iteration level index. I_m is an iteration parameter for the disturbance term in the AIADI scheme. 0.55 is chosen in this work following previous studies (An et al., 2011; Weeks et al., 2004). Each time step is iterated until $|h^{n+1,3m+3}-h^{n+1,3m}|$ is less than the tolerance value given by the user.

2.2. 2D overland flow

Overland flow is simulated using the St. Venant Equations which consists of the continuity equation and two momentum equations. The continuity equation for 2D application is:

$$\frac{\partial W}{\partial t}+\frac{\partial}{\partial x}(Wu)+\frac{\partial}{\partial y}(Wv)-q_i+q_o=0,\tag{7}$$

where W is the depth of water; u and v are velocities in the x and y

direction respectively; and q_i and q_o are the inflow and outflow flux term contributing to the overland flow. These terms, in units of length/time account for sources and sinks in the overland flow process and facilitate the exchange of water between overland and subsurface components of the model. Detailed physical processes included in each term is discussed in section 2.3.

In this work, we use diffusion flow to model the overland flow process. While omitting the inertial terms in the St. Venant Equations, diffusion flow is still capable of accurately representing many natural flow situations (Lal, 1998; Fennema et al., 1994; Akan and Yen, 1981; Hromadka and Lai, 1985). The momentum equations are reduced to:

$$\frac{\partial H}{\partial x} = -S_{fx} \quad \text{and} \quad \frac{\partial H}{\partial y} = -S_{fy}, \tag{8}$$

where $H = W + z$ is the depth of the water, W, in addition to surface elevation, z, above a given datum. Thus, S_{fx}, S_{fy}, the friction slopes are the same as the slope of the water surface S_w in 2D, where $S_w = \sqrt{(S_{fx})^2 + (S_{fy})^2}$. Combined with Manning's equation, flow velocity can be expressed in terms of H (Hromadka and Lai, 1985):

$$u = -\frac{W^{2/3}}{n_m\sqrt{S_w}}\frac{\partial H}{\partial x} = -\frac{D}{h}\frac{\partial H}{\partial x}, \tag{9}$$

$$v = -\frac{W^{2/3}}{n_m\sqrt{S_w}}\frac{\partial H}{\partial y} = -\frac{D}{h}\frac{\partial H}{\partial y}, \tag{10}$$

where n_m is the Manning's coefficient, and D, the diffusion coefficient, is expressed as:

$$D = \begin{cases} \dfrac{W^{5/3}}{n_m\sqrt{S_w}}, & \text{for } |S_w| > S_{min} \quad \text{and} \quad |W| > W_{min} \\ 0, & \text{otherwise} \end{cases}$$

Parameters S_{min} and h_{min} are both user defined. S_{min} is used to keep D within a finite limit, and W_{min} facilitates wetting and drying.

Using Equations (9) and (10), the governing equation, based on continuity (Equation (7)), is written as:

$$\frac{\partial H}{\partial t} = \frac{\partial}{\partial x}\left(D\frac{\partial H}{\partial x}\right) + \frac{\partial}{\partial y}\left(D\frac{\partial H}{\partial y}\right) + q_i - q_o. \tag{11}$$

The overland flow equation can be linearized and solved with a wide variety of approaches (Lal, 1998). In this work, we use a linearized implicit method where Equation (11) is linearized using explicit D and then solved using the implicit backward Euler and finite difference in 2D. Please refer to Appendix A.2 for the discretization of Equation (11).

2.3. Surface-subsurface coupling

Infiltration and evaporation, determined by surface processes and subsurface moisture conditions, couple the overland flow and subsurface components of the 3D flow model. The amount of water exchanged between the two model components is calculated at each timestep. It is included in the sink term in the overland flow model, q_o in Equation (11), and it is a source to the subsurface model by serving as the top boundary condition. We use a switching top boundary condition in the subsurface where, depending on moisture conditions, the top boundary of any cell is Dirichlet or Neumann (Paniconi and Wood, 1993; Camporese et al., 2010, 2014; Sulis et al., 2010; Le et al., 2015). Dirichlet boundary condition applies when infiltration and evaporation becomes limited by soil moisture conditions, such as in the case of saturation excess. Otherwise, Neumann boundary condition applies. Precipitation contributes to the overland flow model through the term q_i from Equation (11), and excess water that does not infiltrate into the soil is included in q_i at the next timestep of the simulation. Additional processes contributing to sources and sinks for the coupled 3D flow model are discussed in Section 3 where the 3D flow model is integrated with a 1D ecohydrologic model.

2.4. Flow model benchmarks

We use a set of benchmarks as preliminary tests for our coupled 3D flow model. These benchmark simulations have been established through previous works and are designed to compare the physical responses of models (Kollet and Maxwell, 2006; Sulis et al., 2010; Maxwell et al., 2014). We use two established test cases, infiltration excess and saturation excess, to examine the most prevalent hydrologic responses and the interaction between overland flow and subsurface flow components of the model.

Both test cases use a domain that slopes in one direction as shown in Fig. 2. The soil depth is 5 m with no water flowing through any boundaries of the domain except the outlet on the right side as depicted in Fig. 2. They both use the same van Genuchten parameters, except for saturated hydraulic conductivity K_s, based on values for sandy-loam soil estimated by Schaap and Leij (1998). Both tests consists of a 300 min simulation that starts with 200 min of rainfall followed by 100 min of recession. Parameters used are shown in Table 1, and the two cases differ in their parameterization for the saturated hydraulic conductivity and initial water table depth as follows:

1. The infiltration excess case tests for runoff before the soil column is saturated due to rainfall rate that is higher than the infiltration rate. Therefore, this case tests two saturated hydraulic conductivity (K_s) values that are smaller than the rainfall rate shown in Table 1.
2. The saturation excess case tests for runoff when the soil column is saturated. This is simulated with a K_s that is larger than the rainfall rate. Two values for initial water table depth are tested given in Table 1.

Fig. 3 compares the outflow rate from our model with that of five other models for the infiltration excess benchmark test case. Our model generally agrees well with other models. Especially for the magnitude of the peak outflow and the recession curve, our model matches other model outputs very closely or is within the range of variability of the other models. The largest discrepancy occurs in the rising limb of the outflow for the low K_s case. Our model produces a slightly steeper rising limb compared to other models tested and thus plateaus faster where the outflow is equivalent to rainfall rate. One possible cause of this is numerical differences in the overland flow model implementation. Another possible cause is the difference in mesh size and timestep for our model. Based on the comparison of a similar test case with different mesh sizes and the analytical solution from Kollet and Maxwell (2006), we see that the analytical solution and simulations with very fine mesh tend to also have a steeper rising limb and plateau faster than models with coarser grids.

Fig. 4 compares the outflow rate from our model with that of other

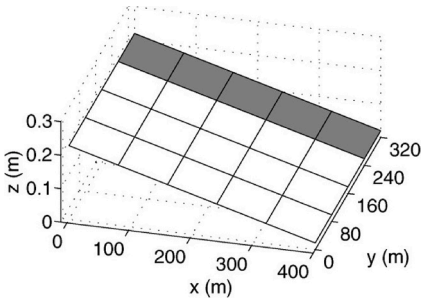

Fig. 2. Domain used for the benchmark tests based on Sulis et al. (2010) and Maxwell et al. (2014). Outflow used for comparison in benchmarks are measured for the gray cells at the bottom of the slope.

Table 1
Parameters used for test cases.

Parameter		Units	Infiltration Excess	Saturation Excess
Horizontal mesh size	$\Delta x = \Delta y$	m	20	20
Vertical mesh size	Δz	m	0.1	0.1
Timestep	Δt	min	0.5	0.5
Initial water table depth	wt	m	1.0	1.0, 0.5
Saturated hydraulic conductivity	K_s	$m\ min^{-1}$	6.94×10^{-5}, 6.94×10^{-6}	6.94×10^{-4}
Porosity	φ	–	0.4	0.4
Specific storage	S_s	m^{-1}	5×10^{-4}	5×10^{-4}
Manning's coefficient[a]	n_m	$m^{-1/3}\ min$	3.31×10^{-4}	3.31×10^{-4}
x direction slope		%	0.05	0.05
y direction slope		%	0	0
Rain rate		$m\ min^{-1}$	3.30×10^{-4}	3.30×10^{-4}
vanGenuchten parameters				
Alpha[a]	α	cm^{-1}	0.01	0.01
Pore-size distribution	n_v	–	2.0	2.0
Residual water content	θ_r	–	0.08	0.08
Saturated water content	θ_s	–	0.4	0.4

[a] Values do not match those of previous publications due to confirmed typos in previous works.

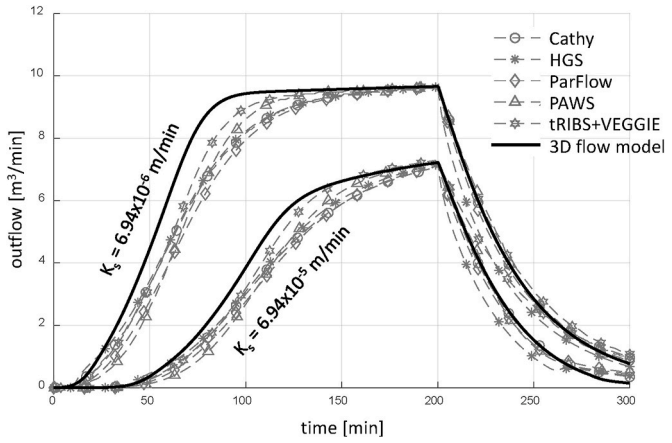

Fig. 3. Comparison of outflow for the infiltration excess test case. Two different values of saturated hydraulic conductivity are tested where our 3D flow model is compared with other similar models. Data of other models are from Maxwell et al. (2014).

models for the saturation excess benchmark test case. Our model also agrees well with other models for this case. Similar to the infiltration excess test case, our model matches other model outputs very closely or

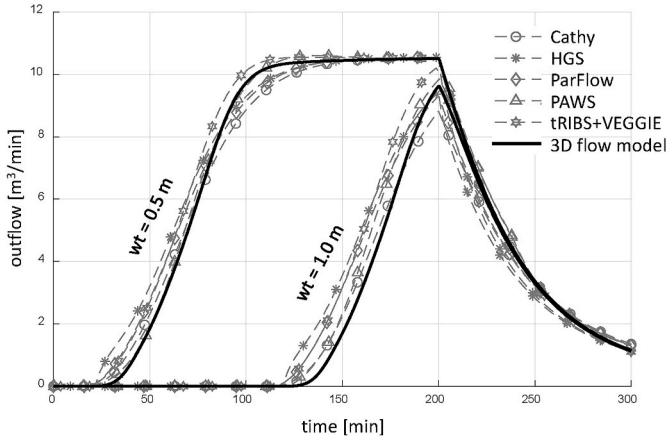

Fig. 4. Comparison of outflow for the saturation excess test case. Two different values of initial water depth are tested where our 3D flow model is compared with other similar models. Data of other models are from Maxwell et al. (2014).

is within the range of variability of the other models for the peak outflow and the recession curve. The largest difference occurs at the rising limb for the case with initial water table at 1.0 m where our model produces outflow slightly slower than other models and have a steeper rising limb similar to the infiltration excess case. Cause for the discrepancy is also likely a combination of differences in numerical implementation and mesh size, same as that of the infiltration excess case. However, in general, results from our model match with other models in the benchmark tests reasonably closely and show expected model behavior which provides confidence in the validity of our model.

3. A virtual laboratory

3.1. Canopy and flow model process integration

In order to simulate land surface processes, we integrate our flow model into the existing Multi-Layer Canopy (MLCan) model (Drewry et al., 2010a,b; Quijano et al., 2012; Le et al., 2012; Quijano et al., 2013; Quijano and Kumar, 2015). MLCan is a high fidelity, high complexity 1D model that simulates above-ground canopy processes by (1) fully coupling leaf biophysical processes including photosynthesis, leaf stomatal conductance, leaf boundary layer conductance and leaf energy balance, (2) scaling from leaf to canopy level with a multi-layer approach using sunlit and shaded leaf fractions for each layer, and (3) resolving the vertical profiles of radiation, water storage, energy balance, and CO_2 flux. MLCan also describes surface and below ground processes such as water storage and energy balance in the litter and snow layers, root and soil water interactions that couples to photosynthesis, soil heat transport, and 1D soil water movement.

We integrate our 3D flow model with MLCan by replacing the original 1D soil moisture model with our 3D subsurface model and adding the 2D overland flow model as shown in Fig. 5. We maintain all process interaction in the original MLCan model such as soil water interactions with plant roots. The transpiration flux, q_t in Equation (4), is modeled as a sink term in the subsurface model, and it is generally uptake of water by plants determined by the canopy transpiration. However, due to the hydraulic redistribution incorporated in the model (Amenu and Kumar, 2008; Quijano et al., 2012), where water travels through plant roots from wet to dry parts of the soil upwards or downwards, q_t can be both sink or source in different parts of the model domain at any timestep.

We also implement additional process interactions with the addition of the 2D overland flow model. Sinks in the overland flow model, q_o from Equation (11), include evaporation and infiltration, as described in Section 2.3, to couple overland flow with subsurface processes. Evaporation from the overland flow model is integrated into MLCan canopy processes. To further integrate the 3D flow model into MLCan surface

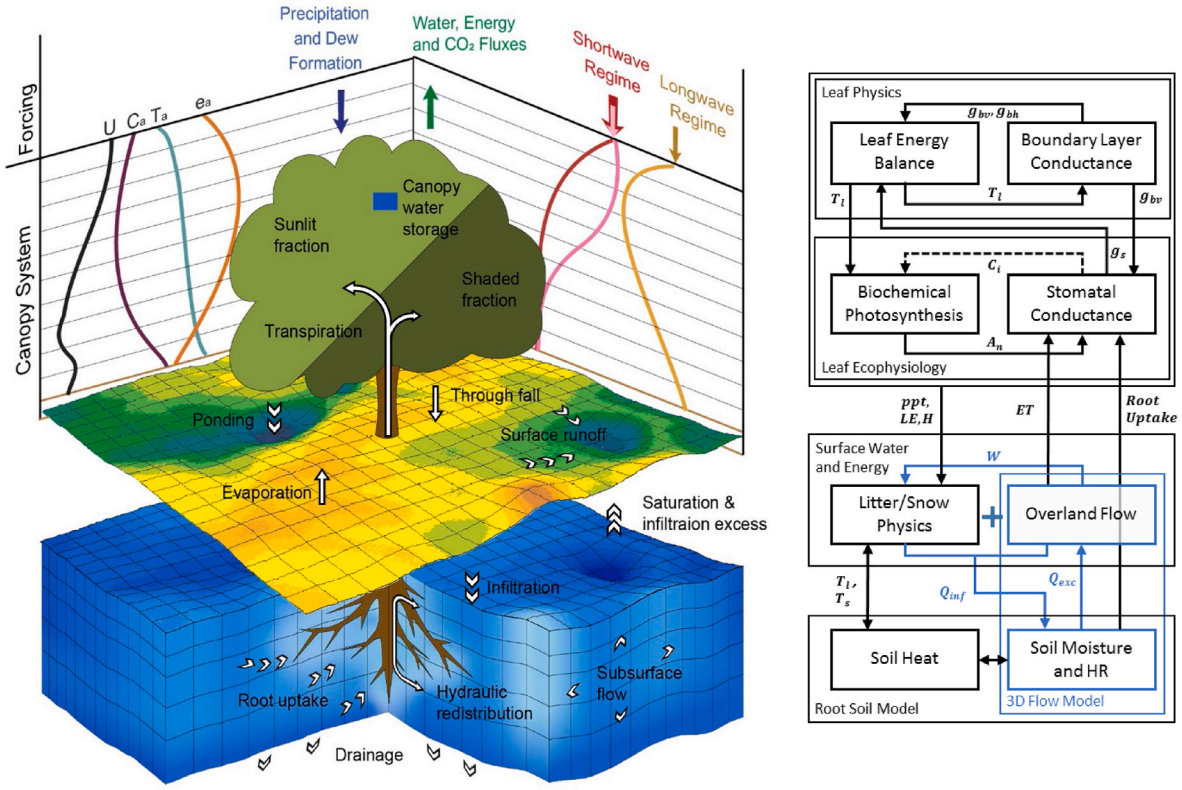

Fig. 5. This figure illustrates the MLCan3D model. The left side is a graphical representation of MLCan3D depicting the integration of the Multi-Layer Canopy model with our new 3D flow model including 2D overland and 3D subsurface flows overlaid with major modeled ecohydrologic processes. The right sides is a schematic showing the coupling of processes in the model with the integration of the 3D flow model into original MLCan shown in blue (adapted from Drewry et al. (2010a); Le et al. (2012)).

and canopy processes, q_o includes the contribution of overland flow to water stored in the litter layer, and precipitation which contributes to q_i from Equation (11) is determined by throughfall from the canopy model and uptake by the litter and snow model. Drainage of excess water from the litter and snow layer, as well as overland flow, contributes to infiltration into the subsurface.

The resulting Multi-layer Canopy and 3D Soil (MLCan3D) model has the capability to represent vegetation dynamics with high fidelity, including acclimation response of vegetation to changes in atmospheric CO_2 (Drewry et al., 2010a,b) and its consequent impact in water and energy partitioning, capture high resolution heterogeneity in the topography and subsurface, and maintains the tight process interactions between vegetation and soil moisture. Fig. 5 shows the schematic of process interactions of the MLCan3D model with the new coupled 3D flow model and associated process interactions highlighted in blue.

3.2. Model capabilities

A detailed physical process model such as MLCan3D inevitably need a lot of data to set up and is computationally demanding. To encourage the use of MLCan3D as a virtual laboratory by the broader scientific community, we develop MLCan3D with an emphasis on accessibility, where the model is easy to set up and understand as well as run without stringent computing hardware constraints.

We use a Graphical User Interface (GUI) to guide users step-by-step through the model setup process. The GUI was first developed for MLCan (Le et al., 2012) and is now modified to include setup of the coupled surface and subsurface flow components. In setting up the model, users first specify the simulation location as latitude and longitude, plant species composition, and vegetation structure through leaf area index (LAI) and vertical leaf area density (LAD) profile for each species. Then, users have the ability to specify which modules to include in the simulation, such as using the 3D flow model (2D overland and 3D subsurface) or the 1D soil moisture module in the original MLCan model. MLCan3D then takes available eddy-covariance flux tower data as model forcings and uses lidar derived Digital Elevation Models (DEMs) to characterize topography for the 3D flow model. For initial soil moisture conditions, users have the option to use a vertical profile that is homogeneous over the domain or input 3D data as a grid of user specified values. Similarly, users can specify 3D heterogeneous soil parameters for soil moisture retention and hydraulic conductivity as described in Equations (2) and (3). Appendix B contains details on how to use the GUI to set up the 3D flow model. MLCan3D outputs water, CO_2, and energy fluxes for the canopy and the soil as well as vegetation dynamics and microclimate conditions. In addition, MLCan3D outputs moisture conditions from the 3D flow model including ponded water depth on the land surface and subsurface soil moisture.

Since we use the Advanced Iterative Alternating Direction Implicit (AIADI) method (An et al., 2011; Douglas and Rachford, 1956) to solve the subsurface flow, the model is significantly less memory intensive than fully implicit methods and is easily parallelized. Therefore, MLCan3D can be run on personal computers for small virtual experiments or in highly parallel computing environments for large experiments. With the help of the GUI and limited hardware constraints,

MLCan3D can be more accessible to users from broader range of backgrounds and encourage virtual experiments to answer more questions from diverse disciplines. MLCan3D is open source and available for download at https://github.com/HydroComplexity/MLCan3D.

4. Model application

MLCan3D can be applied to a wide range of ecosystems. To demonstrate its applicability, we simulate, without calibration, two very different ecosystems to test MLCan3D in real world situations using data from NEON (National Ecological Observatory Network) (National Research Council, 2004). NEON, funded by NSF, consists of a network of long term data collection facilities that provides comprehensive data for quantifying land surface ecological processes. NEON has sites across the US and covers a range of ecosystems and climates. They collect long-term open access data and provide more than 175 data products for ecologic and biological studies, and their standardized data collection and processing protocols can provide comparable data across different sites.

At each NEON site, an eddy covariance flux tower collects weather data needed as forcings for MLCan3D such as radiation, precipitation, air temperature, and wind speed. The tower also collects ecosystem fluxes of water, energy, and carbon which can be used to compare with model output. At each site, there is also an array of soil plots near the tower (Fig. 6) that have sensors at various depths in the soil to measure soil variables such as water content, salinity, and temperature. NEON also collects, processes, and provides high resolution airborne remote sensing data, including hyperspectral, lidar, and digital photography for each site around the time of peak greenness each year. Hyperspectral and lidar remote sensing products are provided at 1 m resolution. The hyperspectral data products include leaf area index (LAI), and lidar data products include canopy height (CHM) and surface elevation (DEM). Observational samples are also taken for a variety of ecosystem factors such as plants, soil, and organisms. Relevant data include plant species, soil texture, and litter layer information. We apply MLCan3D to two sites in order to test model performance for different conditions of vegetation, topography, and soil textures. NEON datasets used to set up model simulations and verify model results are listed in Table 3 in the Appendix.

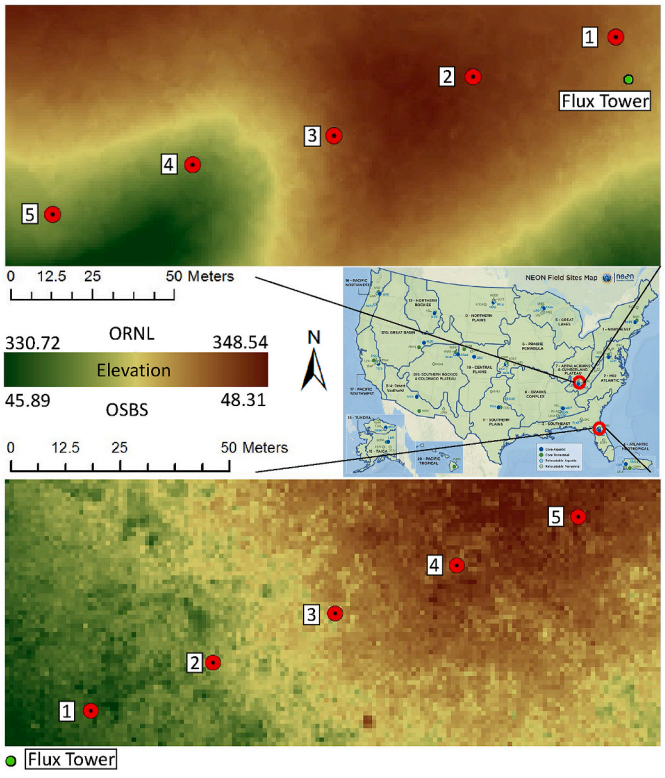

Fig. 6. Illustration of NEON ORNL (top) and OSBS (bottom) sites with their locations on the US map from NEON (NEON, 2020) circled in red. This figure shows the digital elevation model for each site based on Lidar data from NEON (Table 3) and the five soil plots where moisture and temperature measurements are used to compare with model output. The eddy-covariance flux tower locations are also marked.

4.1. Ordway-swisher biological station site

The Ordway-Swisher Biological Station (OSBS) site is located in central Florida (Lat/Long: 29.689 27, −81.993 43). Mean annual precipitation is 1290 mm with more rain in the summer months. It consists of fairly homogeneous evergreen forests dominated by longleaf pine (pinus palustris) within the eddy-covariance flux tower airshed. Average canopy height, based on airborne lidar data, is 23 m with relatively open canopy and low Leaf Area Index (LAI) of 0.79 (ORNL DAAC, 2018a; Myneni et al., 2015).

We use 1 m resolution DEM from airborne Lidar to characterize the topography of the site for the 3D flow model. While the OSBS site has limited elevation changes, it consists of very fast draining deep sandy soils whose sharp changes in soil moisture conditions really test the numerical stability of the subsurface model. According to soil sample measurements, the OSBS soil contains more than 95% sand and is therefore a sandy textured soil. Texture based soil parameters for Equations (2) and (3) found in literature are used as model parameters as shown in Table 2 (Dingman, 2015; Clapp and Hornberger, 1978; Leij, 1996; Ghanbarian-Alavijeh et al., 2010).

In this work, we model a $150 \times 60\ m^2$ plot at $1\ m^2$ resolution covering all soil moisture sensor as shown in Fig. 6. The site has a slight topographic gradient of about 2.5 m going down slope from the north east to the south west. We run the model for June 2018 at 30 min timesteps with a 10 day spin up period. The 3D flow model's initial soil moisture condition is homogeneous with volumetric soil moisture of 0.1, and measured forcing data from May 2018 is used for the spin up period. Due to the fast draining nature of the soil, initial soil moisture conditions do not significantly affect results after the spin up period.

The summary of model results for the simulation period is shown in Fig. 7 where we compare our model simulation with field measured data from NEON. In Fig. 7a, we compare simulated plot-average results of soil moisture and temperature with measured data from five soil plots at 6 cm depth, corresponding to the first layer of 10 cm in our model. We also display the vertical profile of plot-average soil moisture over time. We find that on the plot level average, our model simulation is in good agreement with measured data, though simulated soil temperature does not show diurnal variations as strong as that of the observed data. In Fig. 7b, we show topography of the plot and the heterogeneity of soil moisture over the plot at various depths. Here we observe that simulated soil moisture varies at fine scales that corresponds to heterogeneity due to micro-topographic variability (on the order of a few meters). However, soil moisture does not change significantly over the domain, and the variance of the top layer soil moisture shown in 7b is less than what is observed by the five soil moisture sensors ploted in 7a. This indicates that simulated soil moisture for the OSBS site does not react to larger

scale topographic features, such as the gradual slope in the plot, as much as what the soil moisture sensors measure. In Fig. 7c, we compare diurnally averaged simulated latent heat flux from the plot with that of the measured data from the flux tower. We find that simulated latent heat flux is in good agreement with measured.

4.2. Oak ridge national laboratory site

The Oak Ridge National Laboratory (ORNL) site is located in Tennessee (Lat/Long: 35.964 12, −84.282 6). Mean annual precipitation is 1222 mm with slightly more precipitation in the winter and spring. It consists of mainly mixed deciduous forests dominated by oaks, maples, and hickories within the flux tower airshed with average canopy height of 28 m and LAI of 5.2 (ORNL DAAC, 2018b; Myneni et al., 2015).

As part of the Ridge-and-Valley Appalachians, the site is situated within five parallel ridges and valleys with dramatic variations in elevation. Therefore, this site allows us to test the model's ability to capture the effects of topographic variations. Due to the large topographic variability at the ORNL site, soil texture also varies dramatically from sandy loam and silt loam to clay according to soil sample measurements from NEON. NEON does not have soil sample measurements very close to the eddy-covariance flux tower, but we know from literature and measured data that the soil at the top of the ridges, where the tower is, tends to be more coarse and well drained compared to soil in valleys (Solomon et al., 1992). Therefore, for this study, we use silt loam soil with low porosity as described in Solomon et al. (1992). Texture based soil parameters for Equations (2) and (3) found in literature are shown in Table 2 (Dingman, 2015; Clapp and Hornberger, 1978; Leij, 1996; Ghanbarian-Alavijeh et al., 2010).

For the ORNL site, we model a 200 × 80 m^2 plot at 1 m^2 resolution covering all soil moisture sensor and the eddy-covariance flux tower as shown in Fig. 6. The site has topographic changes of over 17 m over the plot, much larger than that of the OSBS site. We run the model for June 2020 at 30 min timesteps with a 20 day spin up period. Initial soil moisture condition is homogeneous with volumetric soil moisture set to 0.2. To mitigate effects of the initial condition, we use a longer spin up period to compensate for the slower draining soil at the site.

The summary of model results for the simulation period is shown in Fig. 8 where we compare our model simulation with field measured data from NEON. In Fig. 8a, we compare simulated plot-average results of soil moisture and temperature with measured data from five soil plots at 0.06 m depth, corresponding to the first layer of 0.1 m in our model. We find that on the plot level average, our model simulation for the ORNL site is also in good agreement with measured data, though soil moisture does not seem to react as sharply to precipitation as the measured data. Also towards the end of June, simulated soil temperature is slightly lower compared to measured and in general does not see as strong diurnal variations. In Fig. 8b, we show topography of the plot and the heterogeneity of soil moisture over the plot at various depths. Simulated soil moisture is able to capture soil moisture heterogeneity due to large scale topographic gradient as well as micro-topographic variability. However, soil moisture simulation does not show as much spatial variability as is measured by the five soil moisture sensors. In Fig. 8c, we compare diurnally averaged simulated latent heat flux from the plot with that of the measured data from the flux tower. We find that simulated latent heat flux is in good agreement with measured.

5. Discussion and model sensitivities

The canopy component of MLCan3D is strongly affected by vegetation's physical properties and its photosynthetic parameterization. Important physical properties includes LAI and canopy height, which specify the structure of the vegetation. Important photosynthetic parameters, for C3 plants as simulated in our study, include maximum rubisco limited carboxylation rate (V_{cmax}) and maximum electron transport rate (J_{max}).

A few parameters are important in facilitating the interaction of canopy, land surface, and soil. Soil moisture is sensitive to the amount of throughfall, the precipitation that reaches the ground after canopy interception, and the thickness of the surface litter layer since these components directly influence the amount of infiltration. Soil moisture is also affected by root water uptake, as determined by vegetation properties discussed above and conductivity of roots. Manning's coefficient n_m affects the overland flow, and thus influence heterogeneity of infiltration into the subsurface.

Soil moisture is most directly affected by the soil moisture retention curve parameters used in Equations (2) and (3). Simulation results tends to be the most sensitive to K_s where water travels faster through soils with larger K_s, leading to sharper peaks during precipitation and faster drainage. The residual and saturated soil moisture, θ_r, θ_s, are important in bounding the range of soil moisture, and larger θ_s will lead to higher soil moisture, and similarly for θ_r, when all other parameters remain constant. n_v and α also have small affects on soil moisture. Larger n_v leads to drier conditions. Larger α produces slightly higher peaks during precipitation and less dry down, leading to more water retention over time. However, the effect is not very significant when varying α within the reasonable range for the given soil texture.

We parameterize the application cases of our model using parameters found in existing literature when available and do not calibrate the model to fit measured data. From the results, we find that on average, the model can closely estimate soil moisture levels compared to sensor measured values. Vertical movement of moisture in the soil column also seems reasonable from comparing with deeper layer results in the OSBS site. Canopy level latent heat flux is also comparable with measured values. Based on current results, the model performs well in general, but have a few issues that warrants further discussion.

One noticeable difference between the simulated soil moisture and measured soil moisture curves is that sensor measurements register

Table 2
Parameters used for model applications at OSBS and ORNL sites.

Parameter		Units	OSBS	ORNL
Horizontal mesh size	$\Delta x = \Delta y$	m	1	1
Vertical mesh size[a]	Δz	m	0.1 +	0.1 +
Timestep	Δt	hr	0.5	0.5
Saturated hydraulic conductivity	K_s	$m\ hr^{-1}$	0.60	0.026
Porosity	φ	–	0.45	0.40
Specific storage	S_s	m^{-1}	5×10^{-4}	5×10^{-4}
Manning's coefficient	n_m	$m^{-1/3}\ hr$	$4.673\ 5 \times 10^{-6}$	$4.673\ 5 \times 10^{-6}$
vanGenuchten parameters				
Alpha	α	cm^{-1}	0.035	0.01
Pore-size distribution	n_v	–	2.5	1.5
Residual water content	θ_r	–	0.01	0.05
Saturated water content	θ_s	–	0.45	0.40

[a] Vertical mesh size is 0.1 m for the top 1 m of soil, then increases in size as depth increase.

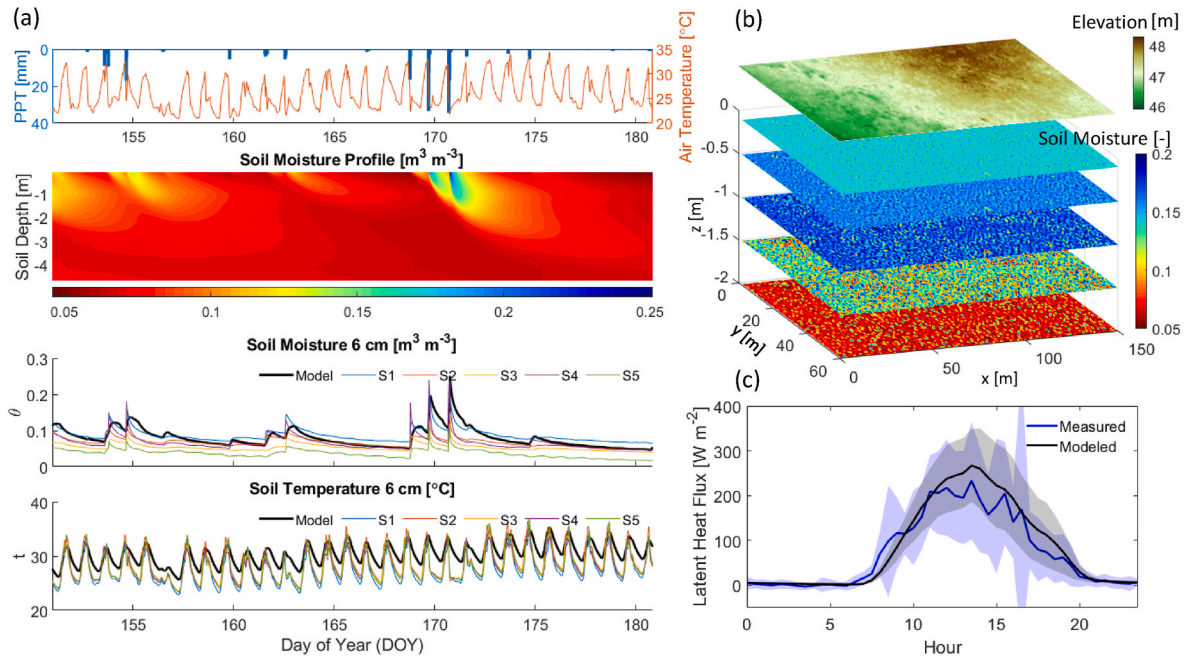

Fig. 7. Comparison of simulation results with measured data for NEON OSBS site. (a) Top two plots show observed precipitation and air temperature, and simulated soil moisture profile over depth for June 2018. Bottom two plots show simulated soil moisture and temperature results for the first soil layer with 10 cm depth compared with measured data from five sensors (S1 to S5 with locations shown in Fig. 6) at 6 cm depth; (b) topography of the simulation domain and simulated soil moisture over the plot at various depths for DOY = 171.2; (c) simulated and measured diurnal latent heat flux averaged over the simulation period with standard deviation shown by the shaded regions.

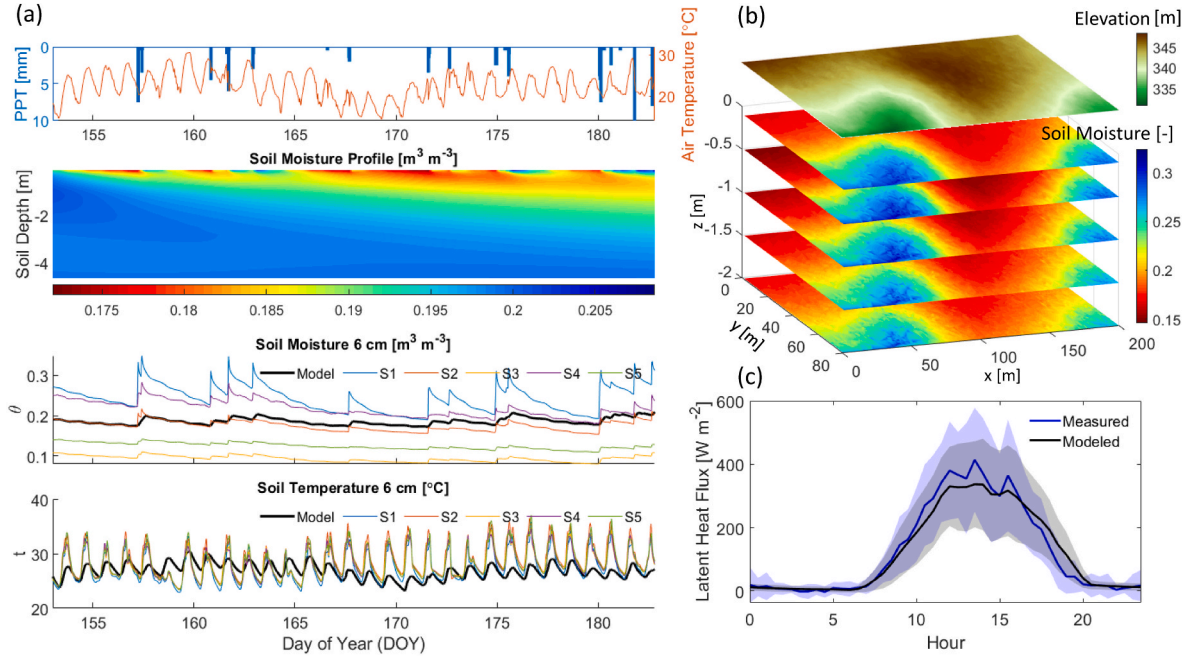

Fig. 8. Comparison of simulation results with measured data for NEON ORNL site. (a) Top two plots show observed precipitation and air temperature, and simulated soil moisture profile over depth for June 2020. Bottom two plots show simulated soil moisture and temperature results for the first soil layer with 10 cm depth compared with measured data from five sensors (S1 to S5 with locations shown in Fig. 6) at 6 cm depth; (b) topography of the simulation domain and simulated soil moisture over the plot at various depths for DOY = 163.4; (c) simulated and measured diurnal latent heat flux averaged over the simulation period with standard deviation shown by the shaded regions.

faster response to precipitation when compared with that of the model simulation. We believe two factors contribute to the more rounded peaks in the simulated soil moisture. One factor is that since the curve is an aggregation of the plot where the variable response from different locations in the plot are averaged, the less sharp peaks reflects the variability within the plot. Another factor is that the modeled canopy and litter layer attenuation of the precipitation signal is not representative of individual sensor locations. If a sensor is not located under vegetation, then it does not experience attenuation of precipitation and will exhibit different behavior compared to locations under vegetation and the average behavior of the plot.

While simulated soil temperature is generally close to measured values, and shows correct diurnal oscillations, the magnitude of simulated oscillations are much less than that of the sensor measurements. This difference may be due to the insulating effects of the litter layer or the limited parameterization of soil heat capacity based on soil texture in the model.

From Figs. 7b and 8b, we see that while micro-topographic effects on soil moisture are evident, the variability of soil moisture across the study plots is not as significant as demonstrated by the measured data. One possibility is that due to the homogeneous initial conditions we currently use for our simulations, soil moisture gradient across each plot has not had time to form during the spin up period. This can be tested with a longer simulation or heterogeneous initial conditions. Another is that there is notable heterogeneity in soil texture that our available data does not capture which influences soil moisture. However, there may also be special unknown conditions influencing individual soil moisture sensors. For example, soil moisture sensor 3 (S3) in the ORNL case measures soil moisture at around 0.1, barely above the residual soil moisture, for the entire duration of the simulation, and does not respond significantly to precipitation. While simulated soil moisture at the location of sensor 3 is drier due to elevation (Fig. 6), this extremely dry soil moisture measurements seems unlikely to be solely caused by topography. Similarly, the low elevation of sensor 5 in the ORNL case (Fig. 6) does not corroborate its low soil moisture measurements and suggests additional factors that can contribute to the large variations we see in soil moisture measurements.

In general, initial simulations using MLCan3D shows that models results are consistent with measured data on average, but do not capture as much variability, both in time and space. This demonstrates there is still a need for further studies to understand and draw connections between in-situ sensors measurements and models simulations. Using MLCan3D as a virtual laboratory, we can conduct virtual experiments that explore this issue. For example, in this work, we find that using topography as the only source of heterogeneity is not enough to capture the variability in the field. We hypothesize that model parameterization may contribute to the discrepancy between measured and modeled soil moisture variability across the study plots. Therefore, we can conduct a virtual experiment using user-specified heterogeneous soil parameters to test this hypothesis.

However, topography is readily available for large extents at high resolutions while soil parameters are not. Therefore, we can also use MLCan3D to ask questions such as how topographic variability interacts with ecohydrologic processes to affect soil moisture and other ecohydrologic fluxes, and to what extent can topography inform heterogeneity in ecohydrologic fluxes. Remotely sensed heterogeneity in vegetation, which leads to variability in throughfall, infiltration, and water uptake, can also be included in future works.

With the ability to model across scales, from micro-topographic to larger scales, and across ecosystems, MLCan3D can also be used to explore how model scale affects heterogeneous ecohydrologic process behaviors and their interactions at different scales. By gaining better understanding and quantification of outstanding scale issues such as how fine scale dynamics amplify or attenuate as scale increases, simulation experiments from MLCan3D can contribute to the hyper-resolution land surface modeling effort in quantifying high resolution heterogeneity over large extents.

6. Conclusion

In this work, we presented MLCan3D, an integrated ecohydrologic model that focuses on high fidelity physical process representation, greater accessibility, and wider applicability. It couples existing advanced ecohydrologic process model MLCan with new state of the art topography aware 3D flow model. MLCan models vegetation, land surface energy fluxes, and above-ground moisture processes. The 3D flow model simulates surface and subsurface moisture dynamics with 2D diffusive overland flow and 3D terrain-following Richards' Equation for subsurface flow. The 3D flow model is in good agreement with other similar models when compared in standard benchmark tests, and when coupled with MLCan, the resulting MLCan3D model enables high resolution ecohydrologic modeling that accounts for micro-topographic variability in the land surface.

To make MLCan3D easily accessible we provide a GUI to facilitate the initialization and the full simulation of the model. We also use the AIADI method for the 3D subsurface flow to reduces computation cost without sacrificing numerical stability. The guidance from the GUI and lack of stringent computing hardware constraints makes MLCan3D more accessible to the general scientific community thus encouraging wider adoption of the model.

We apply MLCan3D to two NEON sites with very different characteristics to demonstrate the broad applicability of the model. Model results are comparable with field measured data at the plot scale and demonstrate the effect of micro-topographic variations on soil moisture. Model simulations did not capture as much heterogeneity as demonstrated by in-situ sensors, a reflection of the fact that topography is not the only source of heterogeneity that contributes to variability of soil moisture in the field. We aim to further explore this result using MLCan3D by investigating additional factors contributing to land surface heterogeneity as well as how topographic variability affects modeled ecohydrologic fluxes.

This work demonstrated the feasibility of using the MLCan3D model as a virtual laboratory that enables a range of virtual experiments by the broader scientific community and contribute to the advancement of our understanding of ecohydrologic process heterogeneity, dynamics, and interactions.

Software and data availability

MLCan3D is written in MATLAB and is tested for MATLAB version R2018b. It is first made available in 2021, requires MATLAB to run and has no strict hardware requirements. MLCan3D is open source and available for education and research uses at https://github.com/HydroComplexity/MLCan3D. Developers' contact information is provided in the MLCan3D readme on GitHub.

Declaration of competing interest

The authors declare that they have no known competing financial interests or personal relationships that could have appeared to influence the work reported in this paper.

Acknowledgment

This work was supported by the National Science Foundation [grant numbers OAC-1835834, EAR-2012850, EAR-1331906, and ACI-1261582]. The authors would like to acknowledge the National Ecological Observatory Network as the source of field measured data used in this work. We would also like to thank professor Reed Maxwell and his students for providing the data for the benchmark comparisons.

Appendix

A. Flow Model Discretization

A.1. Subsurface

Backward Euler scheme is used for the time discretization and finite difference for space discretization. Since the Richards equation is non-linear due to the relationship between θ, K and h, the modified Picard method (Celia et al., 1990) is used to linearize the equation and solve each time step iteratively.

Discretizing Equation (4) with backward Euler and Picard linearization gives:

$$\begin{aligned}&\frac{\theta^{n+1,m+1}-\theta^{n}}{\Delta t}+\frac{\theta^{n+1,m}}{\varphi}\frac{S_s}{\Delta t}\left(h^{n+1,m+1}-h^{n}\right)\\&=\frac{\partial}{\partial x}\left[K^{n+1,m}\left(\left.\frac{\partial h}{\partial x}\right|^{n+1,m+1}\cos\vartheta+\sin\vartheta\right)\right]+\frac{\partial}{\partial y}\left[K^{n+1,m}\left(\left.\frac{\partial h}{\partial y}\right|^{n+1,m+1}\cos\vartheta+\sin\vartheta\right)\right]+\frac{\partial}{\partial z}\left[K^{n+1,m}\left.\frac{\partial h}{\partial z}\right|^{n+1,m+1}\right]-q_t,\end{aligned}\tag{12}$$

where n is the time step, and m is the iteration level of the Picard iteration.

Next, as shown in (Celia et al., 1990), dependent variable $\theta^{n+1,m+1}$ can be written in terms of ψ and h using its Taylor series expansion about $\psi^{n+1,m}$:

$$\theta^{n+1,m+1}=\theta^{n+1,m}+\left.\frac{\partial\theta}{\partial\psi}\right|^{n+1,m}\left(\psi^{n+1,m+1}-\psi^{n+1,m}\right)+\mathcal{O}\left(\delta^2\right)\approx\theta^{n+1,m}+C^{n+1,m}\left(h^{n+1,m+1}-h^{n+1,m}\right)\tag{13}$$

.

Notice that the temporal difference of ψ is equivalent to that of h because the gravitational potential component of h does not change in time and cancels out. Using $C=\frac{\partial\theta}{\partial\psi}$ and with higher order terms omitted, we can plug Equation (13) into Equation (12) to replace $\theta^{n+1,m+1}$:

$$\begin{aligned}&\frac{\theta^{n+1,m}-\theta^{n}}{\Delta t}+\frac{C^{n+1,m}}{\Delta t}\left(h^{n+1,m+1}-h^{n+1,m}\right)+\frac{\theta^{n+1,m}}{\varphi}\frac{S_s}{\Delta t}\left(h^{n+1,m+1}-h^{n}\right)\\&=\frac{\partial}{\partial x}\left[K^{n+1,m}\left(\left.\frac{\partial h}{\partial x}\right|^{n+1,m+1}\cos\vartheta+\sin\vartheta\right)\right]+\frac{\partial}{\partial y}\left[K^{n+1,m}\left(\left.\frac{\partial h}{\partial y}\right|^{n+1,m+1}\cos\vartheta+\sin\vartheta\right)\right]+\frac{\partial}{\partial z}\left[K^{n+1,m}\left.\frac{\partial h}{\partial z}\right|^{n+1,m+1}\right]-q_t.\end{aligned}\tag{14}$$

Applying finite difference, we can write Equation (14) as:

$$\begin{aligned}&\frac{\theta^{n+1,m}_{i,j,k}-\theta^{n}_{i,j,k}}{\Delta t}+\frac{C^{n+1,m}_{i,j,k}}{\Delta t}\left(h^{n+1,m+1}_{i,j,k}-h^{n+1,m}_{i,j,k}\right)+\frac{\theta^{n+1,m}_{i,j,k}}{\varphi_{i,j,k}}\frac{S_s}{\Delta t}\left(h^{n+1,m+1}_{i,j,k}-h^{n}_{i,j,k}\right)\\&=\frac{1}{\Delta x^2}\left[K^{n+1,m}_{i+1/2,j,k}\left(h^{n+1,m+1}_{i+1,j,k}-h^{n+1,m+1}_{i,j,k}\right)\cos\vartheta_{i+1/2,j}-K^{n+1,m}_{i-1/2,j,k}\left(h^{n+1,m+1}_{i,j,k}-h^{n+1,m+1}_{i-1,j,k}\right)\cos\vartheta_{i-1/2,j}\right]+\frac{1}{\Delta x}\left[K^{n+1,m}_{i+1/2,j,k}\sin\vartheta_{i+1/2,j}-K^{n+1,m}_{i-1/2,j,k}\sin\vartheta_{i-1/2,j}\right]\\&+\frac{1}{\Delta y^2}\left[K^{n+1,m}_{i,j+1/2,k}\left(h^{n+1,m+1}_{i,j+1,k}-h^{n+1,m+1}_{i,j,k}\right)\cos\vartheta_{i,j+1/2}-K^{n+1,m}_{i,j-1/2,k}\left(h^{n+1,m+1}_{i,j,k}-h^{n+1,m+1}_{i,j-1,k}\right)\cos\vartheta_{i,j-1/2}\right]+\frac{1}{\Delta y}\left[K^{n+1,m}_{i,j+1/2,k}\sin\vartheta_{i,j+1/2}-K^{n+1,m}_{i,j-1/2,k}\sin\vartheta_{i,j-1/2}\right]\\&+\frac{1}{\Delta z^2}\left[K^{n+1,m}_{i,j,k+1/2}\left(h^{n+1,m+1}_{i,j,k+1}-h^{n+1,m+1}_{i,j,k}\right)-K^{n+1,m}_{i,j,k-1/2}\left(h^{n+1,m+1}_{i,j,k}-h^{n+1,m+1}_{i,j,k-1}\right)\right]-q_t.\end{aligned}\tag{15}$$

A.2. Overland

We linearize Equation (11) by using explicit D and then solved using the implicit Backward Euler and finite difference in 2D. Discretized Equation (11) is written as:

$$\frac{H^{n+1}-H^{n}}{\Delta t}=\frac{1}{\Delta x^2}\left[D^{n}_{i+1/2,j}\left(H^{n+1}_{i+1,j}-H^{n+1}_{i,j}\right)-D^{n}_{i-1/2,j}\left(H^{n+1}_{i,j}-H^{n+1}_{i-1,j}\right)\right]+\frac{1}{\Delta y^2}\left[D^{n}_{i,j+1/2}\left(H^{n+1}_{i,j+1}-H^{n+1}_{i,j}\right)-D^{n}_{i,j-1/2}\left(H^{n+1}_{i,j}-H^{n+1}_{i,j-1}\right)\right]+q_i-q_o,\tag{16}$$

where n is the current timestep.

B. GUI for 3D Flow Model

In this section, we provide details on setting up the 3D flow model, including 2D overland flow and 3D subsurface flow, within MLCan3D. Main steps to set up the 3D flow model include enabling the model in the *Options* window, loading topography data and initial conditions in *Forcing and Initial Conditions* window, then specifying parameters for the model in *Parameters* window. More details on setting up the other model components are discussed in Le et al. (2012).

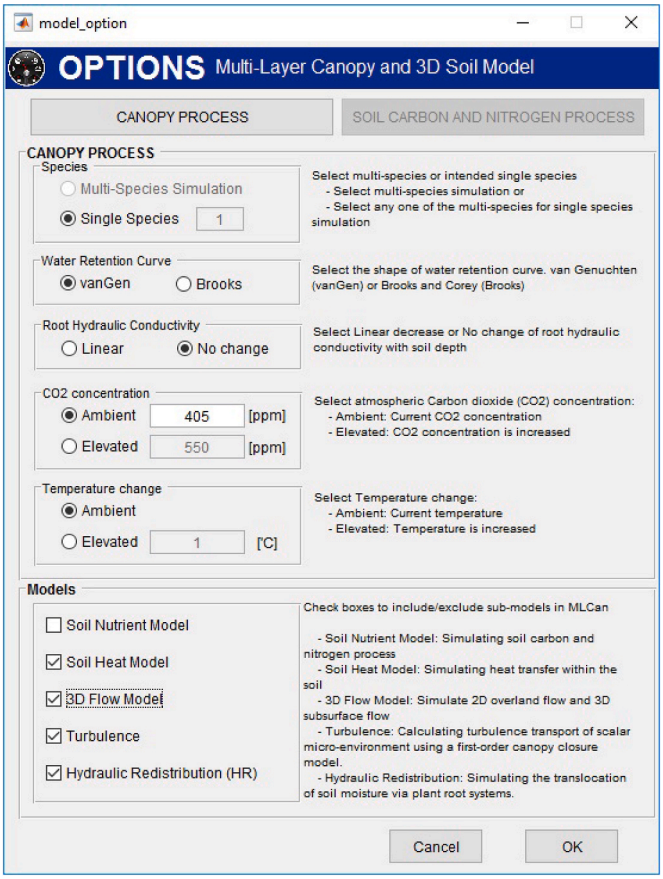

Fig. 9. Screenshot of the model *Options* window. Users can select which model components to include in the simulation, such the 3D Flow Model consisting of 2D overland flow and 3D subsurface flow.

First, to simulate 2D overland flow and 3D subsurface flow, users must enable the *3D Flow Model* option by selecting the model in the *Models* panel within the *Options* window as shown in Fig. 9. This step enables users to proceed to the following steps in setting up the 3D Flow Model. Other subsurface models, including the Nutrient Model, Soil Heat Model, and Hydraulic Redistribution, are coupled with the 1D aggregated soil moisture profile for the domain, and if the *3D Flow Model* checkbox is not selected, soil moisture is simulated in 1D (Amenu and Kumar, 2008; Drewry et al., 2010a; Quijano et al., 2012; Woo and Kumar, 2016).

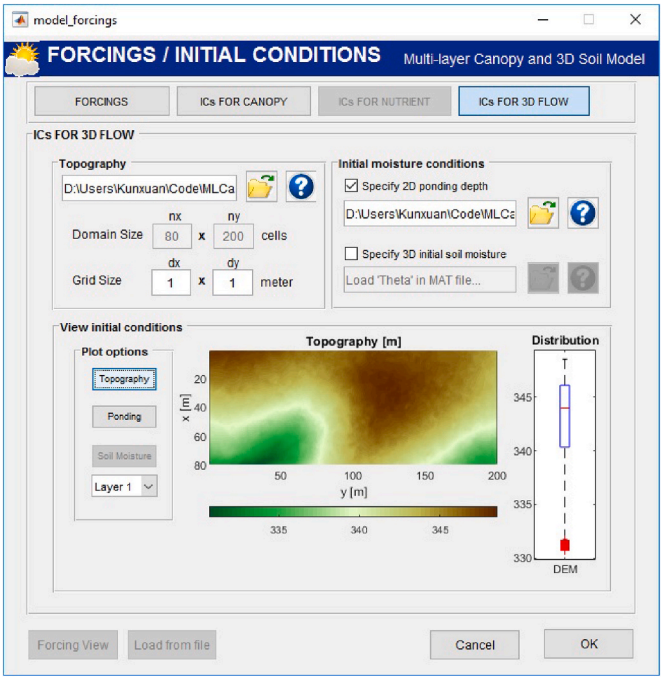

Fig. 10. Screenshot of the model *Forcing and Initial Conditions* window. Here, users must specify topography data, and have the option to use 3D heterogeneous initial conditions. The GUI also provides visualization for the uploaded data.

Once the 3D flow model is enabled, to set up the model, users must first use the *Forcing and Initial Conditions* window to specify the topography of the simulated area (Fig. 10). Topography can be uploaded as a 2D matrix with variable name 'dem' in a .mat file or as a .tiff (or .tif) file. The domain size (*nx*, *ny*) of the simulation is determined based on the size of the uploaded topography data, and the user must specify the size of each grid in meters. The number of layers (*nz*) and the depth of each layer is specified by the root structure earlier in the model setup process (Le et al., 2012). By default, initial conditions for the overland flow assumes no ponded water, and soil moisture is specified as a 1D vertical profile in the *ICs For Canopy* tab found at the top of the window. The 1D profile is then extrapolated to the 3D domain. However, users have the option to specify more complex initial conditions including 2D ponded water depth and 3D soil moisture by checking each option and uploading the corresponding data in .mat files. Details on the file structure requirements can be found by clicking the help buttons at each step. The *View initial conditions* panel provides options to visualize the uploaded data for easy verification of the data.

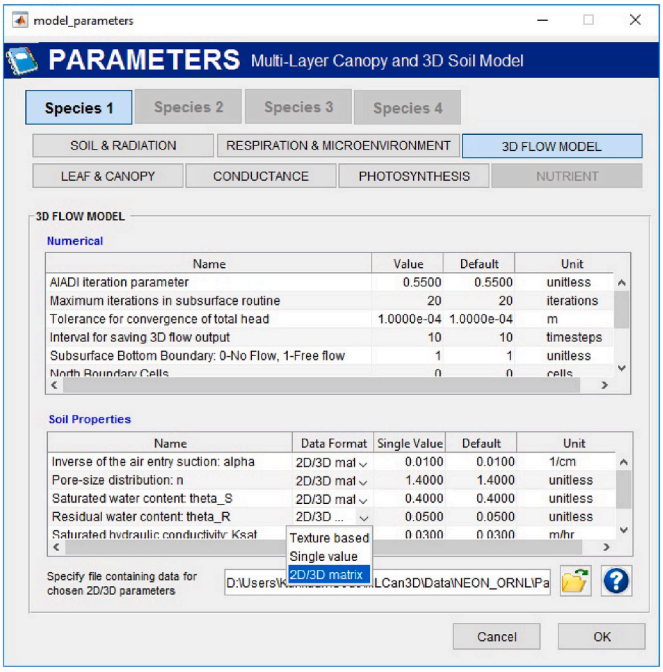

Fig. 11. Screenshot of the model *Parameters* window. Under the *3D FLOW MODEL* tab, users must specify parameters needed in the model

The finial step in setting up the 3D flow model is to specify the parameters used by the 3D flow model in the *3D Flow Model* tab of the *Parameters* window as shown in Fig. 11. There are two main sections for the 3D flow model parameters. The first section includes parameters for the numerical model, such as the maximum number of iterations for the subsurface model, boundary conditions, parallel computing, and how often to save results. Choices for boundary conditions are no flow (0) or free flow (1) for the subsurface bottom boundary, and no flow for side boundaries of the domain. To simulate free flow side boundaries for both overland and subsurface, users can use specify additional boundary cells at each side of the simulation domain. The number of boundary cells can be specified as parameters with value 0, no boundary cells, being the default no flow condition, or any integer for the corresponding number of boundary cells from each edge of the domain. When boundary cells are used, values in those cells are initialized and parameterized similar to other cells in the domain. Their values are also saved in the 3D output so that boundary fluxes can be calculated as needed. However, boundary cells are not considered in the feedback of the 3D flow model with other MLCan3D processes such as root water uptake. Users can also set the number workers used to run the 3D flow model in parallel. Outputs from the 3D flow model, including the depth of ponded water W from equation (7), the soil moisture θ, the total head h, and the hydraulic conductivity $K(\psi)$ from Equation (4) are saved at user defined intervals.

The second section of the *Parameters* window contains detailed specification of parameters for soil moisture retention and hydraulic conductivity as described in Equations (2) and (3). Users have three options for specifying the soil parameters: 1) use the *texture based* option where no additional data input is needed, and the soil parameters are determined based on the soil texture specified by the user during the model setup; 2) use the *single value* option where the entire simulation domain is set to one homogeneous value based on user input; and 3) use the *2D/3D matrix* option where users can specify 3D heterogeneous soil parameters. When using the *2D/3D matrix* option for certain parameters, the user must load a .mat file containing data for each parameter. Help windows and error messages are available to direct users during the setup process.

Table 3
Data sets from NEON used for model applications at OSBS and ORNL as model forcings and model verification.

Data Product ID	Name	OSBS Date Range	ORNL Date Range
DP4.00 200.001	Bundled data products - eddy covariance	2018/05/01–06/30	2020/05/01–06/30
DP1.00 003.001	Triple aspirated air temperature	2018/05/01–06/30	2020/05/01–06/30
DP1.00 004.001	Barometric pressure	2018/05/01–06/30	2020/05/01–06/30
DP1.00 023.001	Shortwave and longwave radiation (net radiometer)	2018/05/01–06/30	2020/05/01–06/30
DP1.00 006.001	Precipitation	2018/05/01–06/30	2020/05/01–06/30
DP1.00 098.001	Relative humidity	2018/05/01–06/30	2020/05/01–06/30
DP1.00 001.001	2D wind speed and direction	2018/05/01–06/30	2020/05/01–06/30
DP1.10 058.001	Plant presence and percent cover	2016/05/01–06/30	2020/06/15 – 06/29
DP3.30 015.001	Ecosystem structure	2018/09	2016/06
DP3.30 024.001	Elevation - LiDAR	2018/09	2016/06
DP1.10 047.001	Soil physical properties (Distributed initial characterization)	2016/03	2016/08
DP1.00 094.001	Soil water content and water salinity	2018/05/01–06/30	2020/05/01–06/30
DP1.00 041.001	Soil temperature	2018/05/01–06/30	2020/05/01–06/30

Table 4
Selection of model vegetation parameters.

Parameter		Units	OSBS	ORNL
Canopy Structure[a]				
Canopy Height	h	m	25	28
Leaf Area Index	LAI	–	0.74	5.2
Foliage clumping factor	Ω	–	1.0	0.9
Flux tower observation height	–	m	35	40
Canopy roughness length	z_0	m	2.5	2.8
Maximum water storage capacity of a leaf	S_m	mm/LAI	0.2	0.3
Leaf Photosynthesis[b]				
Maximum Rubisco limited carboxylation rate at 25°C	$V_{cmax,25}$	$\mu mol/m^2s$	60	80
Maximum electron transport rate at 25°C	$J_{max,25}$	$\mu mol/m^2s$	110	140
Leaf respiration rate at 25°C	$R_{d,25}$	$\mu molCO_2/m^2s$	0.3	0.3
Root Structure[c]				
Root depth	r_d	m	4.5	4.7
50th percentile rooting depth	z_{50}	m	0.6	0.5
95th percentile rooting depth	z_{95}	m	2.5	2

[a] Jensen (2002); Brutsaert (2013); Campbell and Norman (2012); Kitchings and Mann (1976) and NEON eddy covariance (DP4.00 200.001) and ecosystem structure (DP3.30 015.001) data shown in Table 3.
[b] Wright et al. (2013); Sampson et al. (2006); Walker et al. (2014).
[c] Heyward (1933).

References

Akan, A.O., Yen, B.C., 1981. Diffusion-wave flood routing in channel networks. J. Hydraul. Div. 107, 719–732.

Amenu, G., Kumar, P., 2008. A model for hydraulic redistribution incorporating coupled soil-root moisture transport. Hydrol. Earth Syst. Sci. 12, 55–74.

An, H., Ichikawa, Y., Tachikawa, Y., Shiiba, M., 2011. A new iterative alternating direction implicit (iadi) algorithm for multi-dimensional saturated–unsaturated flow. J. Hydrol. 408, 127–139.

Arrigo, J., Salvucci, G., 2005. Investigation hydrologic scaling: observed effects of heterogeneity and nonlocal processes across hillslope, watershed, and regional scales. Water Resour. Res. 41.
Baatz, R., Sullivan, P.L., Li, L., Weintraub, S.R., Loescher, H.W., Mirtl, M., Groffman, P. M., Wall, D.H., Young, M., White, T., et al., 2018. Steering operational synergies in terrestrial observation networks: opportunity for advancing earth system dynamics modelling. Earth Syst. Dyn. 9, 593–609.
Barrios, M., Francés, F., 2012. Spatial scale effect on the upper soil effective parameters of a distributed hydrological model. Hydrol. Process. 26, 1022–1033.
Bear, J., et al., 1979. Groundwater Hydraulics.
Bierkens, M.F., Bell, V.A., Burek, P., Chaney, N., Condon, L.E., David, C.H., de Roo, A., Döll, P., Drost, N., Famiglietti, J.S., et al., 2015. Hyper-resolution global hydrological modelling: what is next? "everywhere and locally relevant". Hydrol. Process. 29, 310–320.
Brantley, S., White, T., White, A., Sparks, D., Richter, D., Pregitzer, K., Derry, L., Chorover, J., Chadwick, O., April, R., Anderson, S., Amundson, R., 2006. Frontiers in Exploration of the Critical Zone: Report of a Workshop Sponsored by the National Science Foundation (NSF), October 24-26, 2005. Newark, DE, p. 30.
Brutsaert, W., 1994. The unit response of groundwater outflow from a hillslope. Water Resour. Res. 30, 2759–2763.
Brutsaert, W., 2013. Evaporation into the Atmosphere: Theory, History and Applications, 1. Springer Science & Business Media.
Callahan, J.T., 1984. Long-term ecological research. Bioscience 34, 363–367. URL: http://www.jstor.org/stable/1309727.
Campbell, G.S., Norman, J., 2012. An Introduction to Environmental Biophysics. Springer Science & Business Media.
Camporese, M., Paniconi, C., Putti, M., Orlandini, S., 2010. Surface-subsurface flow modeling with path-based runoff routing, boundary condition-based coupling, and assimilation of multisource observation data. Water Resour. Res. 46.
Camporese, M., Daly, E., Dresel, P.E., Webb, J.A., 2014. Simplified modeling of catchment-scale evapotranspiration via boundary condition switching. Adv. Water Resour. 69, 95–105.
Celia, M.A., Bouloutas, E.T., Zarba, R.L., 1990. A general mass-conservative numerical solution for the unsaturated flow equation. Water Resour. Res. 26, 1483–1496.
Childs, E., 1971. Drainage of groundwater resting on a sloping bed. Water Resour. Res. 7, 1256–1263.
Clapp, R.B., Hornberger, G.M., 1978. Empirical equations for some soil hydraulic properties. Water Resour. Res. 14, 601–604.
Clark, M.P., Nijssen, B., Lundquist, J.D., Kavetski, D., Rupp, D.E., Woods, R.A., Freer, J. E., Gutmann, E.D., Wood, A.W., Brekke, L.D., et al., 2015. A unified approach for process-based hydrologic modeling: 1. modeling concept. Water Resour. Res. 51, 2498–2514.
Clement, T., Wise, W.R., Molz, F.J., 1994. A physically based, two-dimensional, finite-difference algorithm for modeling variably saturated flow. J. Hydrol. 161, 71–90.
de Graaf, I.E., van Beek, R.L., Gleeson, T., Moosdorf, N., Schmitz, O., Sutanudjaja, E.H., Bierkens, M.F., 2017. A global-scale two-layer transient groundwater model: development and application to groundwater depletion. Adv. Water Resour. 102, 53–67.
Dingman, S.L., 2015. Physical Hydrology. Waveland press.
Douglas, J., Rachford, H.H., 1956. On the numerical solution of heat conduction problems in two and three space variables. Trans. Am. Math. Soc. 82, 421–439.
Drewry, D., Kumar, P., Long, S., Bernacchi, C., Liang, X.Z., Sivapalan, M., 2010a. Ecohydrological responses of dense canopies to environmental variability: 1. interplay between vertical structure and photosynthetic pathway. J. Geophys. Res.: Biogeosciences 115.
Drewry, D.T., Kumar, P., Long, S., Bernacchi, C., Liang, X.Z., Sivapalan, M., 2010b. Ecohydrological responses of dense canopies to environmental variability: 2. role of acclimation under elevated co2. J. Geophys. Res.: Biogeosciences 115.
Dunne, T., Zhang, W., Aubry, B.F., 1991. Effects of rainfall, vegetation, and microtopography on infiltration and runoff. Water Resour. Res. 27, 2271–2285.
Fatichi, S., Vivoni, E.R., Ogden, F.L., Ivanov, V.Y., Mirus, B., Gochis, D., Downer, C.W., Camporese, M., Davison, J.H., Ebel, B., et al., 2016. An overview of current applications, challenges, and future trends in distributed process-based models in hydrology. J. Hydrol. 537, 45–60.
Fennema, R.J., Neidrauer, C.J., Johnson, R.A., MacVicar, T.K., Perkins, W.A., 1994. A computer model to simulate natural everglades hydrology. Everglades: the ecosystem and its restoration 249–289.
Frei, S., Fleckenstein, J.H., 2014. Representing effects of micro-topography on runoff generation and sub-surface flow patterns by using superficial rill/depression storage height variations. Environ. Model. Software 52, 5–18.
Frei, S., Lischeid, G., Fleckenstein, J., 2010. Effects of micro-topography on surface–subsurface exchange and runoff generation in a virtual riparian wetland—a modeling study. Adv. Water Resour. 33, 1388–1401.
Ghanbarian-Alavijeh, B., Liaghat, A., Huang, G.H., Van Genuchten, M.T., 2010. Estimation of the van genuchten soil water retention properties from soil textural data. Pedosphere 20, 456–465.
Heyward, F., 1933. The root system of longleaf pine on the deep sands of western Florida. Ecology 14, 136–148.
Hillel, D., 2013. Fundamentals of Soil Physics. Academic press.
Hromadka II, T., Lai, C., 1985. Solving the two-dimensional diffusion flow model. In: Hydraulics and Hydrology in the Small Computer Age, Proceedings of the Specialty Conference, pp. 555–562.
Jensen, R.R., 2002. Spatial and temporal leaf area index dynamics in a north central Florida, USA preserve. Geocarto Int. 17, 47–54.
Kitchings, T., Mann, L., 1976. Description of the Terrestrial Ecology of the Oak Ridge Environmental Research Park. Technical Report. Oak Ridge National Lab.
Kollet, S.J., Maxwell, R.M., 2006. Integrated surface–groundwater flow modeling: a free-surface overland flow boundary condition in a parallel groundwater flow model. Adv. Water Resour. 29, 945–958.
Lal, A.W., 1998. Performance comparison of overland flow algorithms. J. Hydraul. Eng. 124, 342–349.
Le, P.V., Kumar, P., 2017. Interaction between ecohydrologic dynamics and microtopographic variability under climate change. Water Resour. Res. 53, 8383–8403.
Le, P.V., Kumar, P., Drewry, D.T., Quijano, J.C., 2012. A graphical user interface for numerical modeling of acclimation responses of vegetation to climate change. Comput. Geosci. 49, 91–101.
Le, P.V., Kumar, P., Valocchi, A.J., Dang, H.V., 2015. Gpu-based high-performance computing for integrated surface–sub-surface flow modeling. Environ. Model. Software 73, 1–13.
Leij, F.J., 1996. The UNSODA Unsaturated Soil Hydraulic Database: User's Manual, 96. National Risk Management Research Laboratory, Office of Research and ….
Maxwell, R.M., 2013. A terrain-following grid transform and preconditioner for parallel, large-scale, integrated hydrologic modeling. Adv. Water Resour. 53, 109–117.
Maxwell, R.M., Putti, M., Meyerhoff, S., Delfs, J.O., Ferguson, I.M., Ivanov, V., Kim, J., Kolditz, O., Kollet, S.J., Kumar, M., et al., 2014. Surface-subsurface model intercomparison: a first set of benchmark results to diagnose integrated hydrology and feedbacks. Water Resour. Res. 50, 1531–1549.
Maxwell, R., Condon, L., Kollet, S., 2015. A high-resolution simulation of groundwater and surface water over most of the continental us with the integrated hydrologic model parflow v3. Geosci. Model Dev. (GMD) 8, 923.
McGrath, G.S., Paik, K., Hinz, C., 2012. Microtopography alters self-organized vegetation patterns in water-limited ecosystems. J. Geophys. Res.: Biogeosciences 117.
Mualem, Y., 1976. A new model for predicting the hydraulic conductivity of unsaturated porous media. Water Resour. Res. 12, 513–522.
Myneni, R., Knyazikhin, Y., Park, T., 2015. Mcd15a2h Modis/terra+aqua Leaf Area Index/fpar 8-day L4 Global 500m Sin Grid V006. NASA EOSDIS Land Processes DAAC. https://doi.org/10.5067/MODIS/MCD15A2H.006.
National Research Council, 2004. Neon: Addressing the Nation's Environmental Challenges. The National Academies Press, Washington, DC. https://doi.org/10.17226/10807. URL: https://www.nap.edu/catalog/10807/neon-addressing-the-nations-environmental-challenges.
NEON, (National Ecological Observatory Network), 2020. Field Sites Map. https://www.neonscience.org/sites/default/files/FieldSitesMap-36x24-Poster.pdf. (Accessed 19 November 2020).
Nykanen, D.K., Foufoula-Georgiou, E., 2001. Soil moisture variability and scale-dependency of nonlinear parameterizations in coupled land–atmosphere models. Adv. Water Resour. 24, 1143–1157.
ORNL DAAC, 2018a. Fixed Sites Subsetting and Visualization Tool. ORNL DAAC, Oak Ridge, Tennessee, USA. https://doi.org/10.3334/ORNLDAAC/1567. Subset obtained for MCD15A2H product at site id 'us_florida_neon_osbs'. (Accessed 5 August 2020).
ORNL DAAC, 2018b. Fixed Sites Subsetting and Visualization Tool. ORNL DAAC, Oak Ridge, Tennessee, USA. https://doi.org/10.3334/ORNLDAAC/1567. Subset obtained for MCD15A2H product at site id 'us_tennessee_neon_ornl'. (Accessed 9 June 2021).
Paniconi, C., Wood, E.F., 1993. A detailed model for simulation of catchment scale subsurface hydrologic processes. Water Resour. Res. 29, 1601–1620.
Peaceman, D.W., Rachford Jr., H.H., 1955. The numerical solution of parabolic and elliptic differential equations. J. Soc. Ind. Appl. Math. 3, 28–41.
Quijano, J.C., Kumar, P., 2015. Numerical simulations of hydraulic redistribution across climates: the role of the root hydraulic conductivities. Water Resour. Res. 51, 8529–8550.
Quijano, J.C., Kumar, P., Drewry, D.T., Goldstein, A., Misson, L., 2012. Competitive and mutualistic dependencies in multispecies vegetation dynamics enabled by hydraulic redistribution. Water Resour. Res. 48.
Quijano, J.C., Kumar, P., Drewry, D.T., 2013. Passive regulation of soil biogeochemical cycling by root water transport. Water Resour. Res. 49, 3729–3746.
Riley, W., Shen, C., 2014. Characterizing coarse-resolution watershed soil moisture heterogeneity using fine-scale simulations. Hydrol. Earth Syst. Sci. 18, 2463.
Rubin, J., 1968. Theoretical analysis of two-dimensional, transient flow of water in unsaturated and partly unsaturated soils 1. Soil Sci. Soc. Am. J. 32, 607–615.
Sampson, D., Waring, R., Maier, C., Gough, C., Ducey, M.J., Johnsen, K., 2006. Fertilization effects on forest carbon storage and exchange, and net primary production: a new hybrid process model for stand management. For. Ecol. Manag. 221, 91–109.
Schaap, M.G., Leij, F.J., 1998. Database-related accuracy and uncertainty of pedotransfer functions. Soil Sci. 163, 765–779.
Shukla, J., Nobre, C., Sellers, P., 1990. Amazon deforestation and climate change. Science 247, 1322–1325.
Sloan, P.G., Moore, I.D., 1984. Modeling subsurface stormflow on steeply sloping forested watersheds. Water Resour. Res. 20, 1815–1822.
Solomon, D., Toran, L., Dreier, R., Moore, G., McMaster, W., 1992. Status Report: A Hydrologic Framework for the Oak Ridge Reservation. Technical Report. Oak Ridge National Lab.
Sulis, M., Meyerhoff, S.B., Paniconi, C., Maxwell, R.M., Putti, M., Kollet, S.J., 2010. A comparison of two physics-based numerical models for simulating surface water–groundwater interactions. Adv. Water Resour. 33, 456–467.
Sutanudjaja, E.H., Van Beek, R., Wanders, N., Wada, Y., Bosmans, J.H., Drost, N., Van Der Ent, R.J., De Graaf, I.E., Hoch, J.M., De Jong, K., et al., 2018. Pcr-globwb 2: a 5 arcmin global hydrological and water resources model. Geosci. Model Dev. (GMD) 11, 2429–2453.

Thompson, S.E., Katul, G.G., Porporato, A., 2010. Role of microtopography in rainfall-runoff partitioning: an analysis using idealized geometry. Water Resour. Res. 46.
Van Genuchten, M.T., 1980. A closed-form equation for predicting the hydraulic conductivity of unsaturated soils 1. Soil Sci. Soc. Am. J. 44, 892–898.
Vivoni, E.R., Rodríguez, J.C., Watts, C.J., 2010. On the spatiotemporal variability of soil moisture and evapotranspiration in a mountainous basin within the north american monsoon region. Water Resour. Res. 46.
Walker, J., Rowntree, P., 1977. The effect of soil moisture on circulation and rainfall in a tropical model. Q. J. R. Meteorol. Soc. 103, 29–46.
Walker, A., Aranda, I., Beckerman, A., Bown, H., Cernusak, L., Dang, Q., Domingues, T., Gu, L., Guo, S., Han, Q., Kattge, J., Kubiske, M., Manter, D., Merilo, E., Midgley, G., Porte, A., Scales, J., Tissue, D., Turnbull, T., Warren, C., Wohlfahrt, G., Woodward, F., Wullschleger, S., 2014. A global data set of leaf photosynthetic rates, leaf n and p, and specific leaf area. URL: http://daac.ornl.gov/cgi-bin/dsviewer.pl?ds_id=1224.
Weeks, S.W., Sander, G.C., Braddock, R.D., Matthews, C.J., 2004. Saturated and unsaturated water flow in inclined porous media. Environ. Model. Assess. 9, 91–102.
Woo, D.K., Kumar, P., 2016. Mean age distribution of inorganic soil-nitrogen. Water Resour. Res. 52, 5516–5536.
Wood, E.F., Roundy, J.K., Troy, T.J., Van Beek, L., Bierkens, M.F., Blyth, E., de Roo, A., Döll, P., Ek, M., Famiglietti, J., et al., 2011. Hyperresolution global land surface modeling: meeting a grand challenge for monitoring earth's terrestrial water. Water Resour. Res. 47.
Wright, J., Williams, M., Starr, G., McGee, J., Mitchell, R., 2013. Measured and modelled leaf and stand-scale productivity across a soil moisture gradient and a severe drought. Plant Cell Environ. 36, 467–483.